



# Improvement in fatigue strength of 41Cr4 steel through slide diamond burnishing

J. T. Maximov<sup>1</sup> · G. V. Duncheva<sup>1</sup> · A. P. Anchev<sup>1</sup> · V. P. Dunchev<sup>1</sup> · M. D. Ichkova<sup>1</sup>

Received: 18 September 2019 / Accepted: 13 March 2020 / Published online: 26 March 2020  
© The Brazilian Society of Mechanical Sciences and Engineering 2020

## Abstract

Slide burnishing (SB) is a static mechanical surface treatment based on the severe plastic deformation of the surface for which the contact between the deforming element and the surface being treated is sliding friction. SB improves the surface integrity of metal structural and machine components dramatically. This paper is devoted to improving the fatigue strength of 41Cr4 steel hourglass-shaped specimens subjected to SB with a spherical-ended deforming diamond via different combinations of basic governing parameters. Since the residual compressive stresses introduced play a significant role for the fatigue behavior of the burnished components, a comprehensive parametric study of the SB process was conducted using fully coupled thermal-stress finite element (FE) simulations. The FE model's adequacy was proven via comparison of the FE results for the residual stresses with X-ray diffraction measurements. The results obtained show that the diamond radius and the burnishing force have the strongest effects on the residual stresses, which, in turn, have a significant influence on the fatigue strength, respectively, fatigue life. An extensive experimental investigation of the effect of the selected SB basic parameters on the fatigue limit of the slide burnished specimens was carried out using Locatti's method. The latter is based on the Palmgren–Miner linear damage hypothesis, which is a particular case of a general cumulative damage theory. A planned experiment was carried out, with the governing factors changed among four levels. Regression analysis of the experimental results was carried out, and a model for predicting the fatigue limit was obtained. Based on the model obtained, a one-purpose optimization was carried out using a genetic algorithm. By means of the optimal basic parameters, the fatigue limit of the processed specimens was increased by 22.7%—from 440 to 540 MPa. The fatigue life increased more than 100 times over after SB with the optimal basic parameters.

**Keywords** Slide burnishing · Fully coupled thermal-stress FEM analysis · Residual stresses · Surface integrity · Fatigue limit

## List of symbols

$A$	Amplitude	$\bar{k}$	Number of stress amplitudes
$A_5$	Elongation	$K_{ij}$	Submatrices
$B$	Amplitude	$n_i$	Base number of cycles
$b$	Rate of yield surface size change	$N$	Number of cycles to failure
$C$	Kinematic hardening modulus	$q_g$	Heat flux density
$d_p$	Depth of penetration	$Q_\infty$	Maximum change in the yield surface size
$E$	Young's modulus	$r$	Deforming diamond radius
$f$	Feed rate	$R$	Cycle asymmetry factor
$F_b$	Burnishing force	$R_T$	Thermal residual vector
$k$	Conductivity	$R_u$	Mechanical residual vector
		$R_w$	Workpiece radius
		$s$	Slip
		$t$	Time
		$t^*$	Total time
		$T^*$	Total time in the enlarged FE model
		$T$	Temperature
		$u$	Displacement

Technical Editor: Izabel Fernanda Machado.

✉ J. T. Maximov  
jordanmaximov@gmail.com

<sup>1</sup> Technical University of Gabrovo, 5300 Gabrovo, Bulgaria

$v$	Burnishing velocity
$x_i$	Codded coordinate
$z_t$	Transverse contraction
$\alpha_{ij}$	Back-stress tensor
$\alpha_t$	Coefficient of thermal expansion
$\gamma$	Rate of decrease of $C$
$\bar{\epsilon}^{pl}$	Equivalent plastic strain
$\varphi$	Full angle of rotation
$\varphi_i$	Coefficients
$\eta$	Coefficient
$\mu$	Friction coefficient
$\nu$	Poisson's ratio
$\rho$	Density
$\sigma_{-1}$	Fatigue limit
$\sigma_a$	Stress amplitude
$\sigma_{ij}$	Stress tensor
$\sigma_{ij}^a$	Active stress tensor
$\sigma^0$	Equivalent stress
$\sigma_u$	Ultimate stress
$\sigma _0$	Yield limit
$\theta$	Angle of the workpiece portion segment
$\theta_0$	Initial angle
$\tau$	Friction stress
$\omega$	Angular velocity

## 1 Introduction

Slide burnishing (SB) is a static mechanical surface treatment for which the contact between the deforming element and the surface being treated is sliding friction. SB is especially suitable for finishing rotating metal components. From the kinematics point of view, SB is similar to turning. Instead of a cutting tip, a deforming element (usually a synthetic diamond), typically with a spherical end, is used. The governing SB parameters are basic and additional. The basic parameters are the sphere radius  $r$  of the deforming element, burnishing force  $F_b$ , feed rate  $f$  and burnishing velocity  $v$ . The number of passes, working scheme and use of lubricants are additional parameters. An important advantage is that SB is implemented with simple devices on conventional and CNC lathe machine tools. Hereof, SB is a cost-effective process which avoids costly supplementary processes such as grinding and honing and therefore has less impact on the environment.

Due to the sliding friction contact between the deforming element and the surface being treated, the nature of the SB process is different from those of roller burnishing or deep rolling processes. The heat source in SB is due to the friction and plastic deformation in the contact zone. Regardless of the low friction coefficient resulting from using a synthetic diamond as a deforming element, the work of the

friction forces is significant and dissipates into heat. It can be expected that the pressure and burnishing velocity will have the greatest influence on the contact field temperature. The pressure depends on the burnishing force (whose direction is normal to the cylindrical surface being processed) and the deforming element radius. At constant burnishing force, it can be assumed that a reduction in the radius leads to a reduction in the contact size, leading in turn to increasing contact pressure, and thus to increasing generated heat flow density. The time the heat source spends in the vicinity of a point from (action time) from the surface to be treated with SB depends on the magnitude of the contact area and the burnishing velocity. For instance, when the velocity is  $v = 100$  m/min, the action time is less than one millisecond. Very short action times and large heat flow densities cause intense heating in the vicinity of a point on the surface layer. The joint action of the temperature and force factors causes severe plastic deformation, characterized by a very large gradient in a depth from the surface layer. Unlike the roller burnishing and deep rolling processes, the tangential components of the surface plastic strain are significant in the SB process. This is the physical basis for the so-called micro-effect in SB process. Based on the severe surface plastic deformation, it has been proved that the SB process produces two main effects [1], each of which leads to increased fatigue strength. The micro-effect is expressed in the modification of the microstructure of the surface and subsurface layers and leads to increased plasticity and fatigue crack resistance. The macro-effect is expressed in the creation of beneficial residual stresses in the surface and subsurface layers. The residual compressive stresses retard the formation and growth of fatigue macro-cracks and thus increase the fatigue strength. The combination of the two effects predetermines the fatigue behavior of the processed component. In fact, SB is implemented with a specific combination of basic and additional process parameters. Each combination defines a specific SB process. As a result, a specific residual stress profile and surface microstructure is obtained. Therefore, each combination of these parameters defines the specific fatigue behavior of the corresponding component.

It can be assumed that the combination of high speed and large burnishing force, along with a small radius and a small feed rate, will result in a maximum temperature. The high contact temperature causes deterioration in the SI and accelerates wear on the diamond deforming element. In principle, the heat generated causes the emergence of thermo-plastic deformations, which influence the formation of the residual stress field. For instance, it has been demonstrated experimentally via the X-ray diffraction technique that SB of stainless steel with high burnishing velocity reduced significantly the compressive residual stress on the surface to a depth up to 0.15 mm [2]. Therefore, the assignment of optimal values for the governing parameters for the SB process

must take into account that the temperature factor allows improvements in SI. Thus, the load-bearing capacity and fatigue life of the respective component can be increased significantly. Due to the above-mentioned features of the thermal process in SB (a very short heat source exposure time, a very small contact area, and a very large temperature gradient at a depth from the surface), an experimental determination of the temperature is very difficult. The tracking of the formation and alteration of the residual stresses in real time is practically impossible to do experimentally. In principle, it is possible to apply an analytical approach to 3D thermal analysis. However, when the analysis is extended to the formation of the stressed state in the vicinity of a point, the analytical approach is doomed to failure. Therefore, in this study, fully coupled thermal-stress finite element (FE) analysis was implemented to study the effect of SB parameters on the residual stress profile formation. The residual compressive stresses (as in magnitude and depth of distribution) introduced by SB are crucial for increasing the fatigue strength of the processed components.

The main objective of this study is to establish the combination of the basic parameters of the SB process which provides a maximum fatigue limit for a processed component made of 41Cr4 steel. The study was conducted in four successive stages: (1) comprehensive analysis of the thermal–mechanical nature of the SB process using fully coupled thermal-stress FE analysis in order to establish the influence of the heat generated on the strained and stressed state of the surface and subsurface layers; (2) selection of the significant SB process parameters necessary for forming a residual stress profile and stress ranges of variation; (3) experimental determination of the fatigue limit of specimens slide burnished with various combinations of significant factors; and (4) SB process optimization under the “maximum fatigue limit” criterion.

## 2 Literary survey

A detailed analysis of the studies (analytical, numerical and experimental) done on SB was made by Maximov et al. [3]. The analysis indicated that the basic approach to studying SB was experimental (74%). The FE approach is used considerably less—only 10% of the published studies use an FE method (FEM). It should be noted that the FEM has been used more extensively to explore the processes involved in rolling contact, i.e., roller burnishing [4–15] and deep rolling [16–30] (including the special case of deep rolling—low plasticity burnishing [31–37]), than for SB study [38–46]. When it comes to SB, the case in which the deforming element is a diamond is most often simulated [38, 40–44, 46]. In [39], the FEM was applied to spherical motion burnishing. Teimouri et al. [45] used the FEM to simulate

ultrasonic-assisted slide burnishing. The object of study was most often the residual stresses introduced [38–45], but roughness [39], displacements [39, 46], strains [39, 46] and temperature [44] made appearances as well. The materials studied were: Ti-6Al-4V [38], 37Cr4 steel [39, 44], 41Cr4 steel [40], 2024-T3 Al alloy [41, 43], R260 rail steel [42], 6061-T6 Al alloy [45] and 20X steel [46]. 2D plane strain [38, 39, 46] as well as 3D [40, 41, 43–45] FE models were used. Both 2D and 3D FE models were used in [42], and the result obtained were compared with the experimental results for the residual stresses. The deforming element has been modeled as a deformable solid [38, 44, 45] or rigid body (analytically rigid) [39–43, 46]. The modeled portion of the workpiece had an elastic–plastic behavior. The initial roughness (before SB) was taken into consideration in [39, 40, 42, 44]. SB, as well as the rest of the burnishing methods, acts on the surface and subsurface layers of the workpiece to a relatively small depth (under 1 mm). Therefore, the constitutive model of these layers in the plastic field and the strain hardening model are crucial for the accuracy of the results obtained. The constitutive model has been most often based on an indentation test (affecting only surface and subsurface layers) [39–41, 43, 44, 46]. Only in [44] was a temperature-dependent constitutive model obtained and fully coupled thermal-stress FE analysis conducted. Given the cyclic loading of the surface layer in the SB process, nonlinear kinematic [41–43] and nonlinear kinematic/isotropic hardening [39, 40, 44] were most commonly used. Regardless of the peculiarities of behavior exhibited by cyclically loaded plastic material, some authors have used isotropic hardening [46], as well as the Johnson–Cook model [45], which also defines isotropic hardening. Two methods of setting the movement of the deforming element relative to the workpiece were used: simplified (“loading–unloading–feed”) [38, 41, 43] and accurate (sliding on a cylindrical surface) [40, 42, 44]. A variant of the simplified method, sliding along a plane, was used in [46]. The complex movement, a superposition of spherical motion and translation, in spherical motion burnishing was replaced by a plane motion based on approximate kinematic theory [39]. Most often ABAQUS FEM software (both solvers—explicit and implicit) was used [39–45].

Based on this survey, the following conclusion can be made. To build an adequate FEM model, five basic prerequisites are necessary: (1) a realistic geometry of the modeled portion of the workpiece surface layer; (2) an appropriate creation of the FEM mesh; (3) a realistic interaction between the deforming tool and the workpiece; (4) adequate thermo-mechanical boundary conditions; and (5) an adequate constitutive thermo-mechanical model of the surface and the subsurface layers, where the model is established in a manner that corresponds to the actual loading of these layers. The experimental studies of SB mainly focused on studying the SI obtained (85%), while

the performance of SB-treated specimens occupies only 10% of the studies, of which 46% concern fatigue behavior, i.e., only 4.6% of the studies are devoted to the fatigue behavior of the components processed via SB [3]. The effect of SB on the fatigue strength of steel specimens was investigated by: Aliev and Aslanov [47] for stainless steel, Korzynski et al. [48] for 42CrMo4 steel, Korzynski et al. [49] for 42CrMo4 and 41Cr4 steels with chromium coatings, Maximov et al. [40] for 42Cr4 steel, Maximov et al. [50] for 37Cr4 steel, Swirad [51] for 40HM steel and Maximov et al. [2] for AISI 316Ti steel. As can be seen, there are no studies devoted to 41Cr4 steel without chromium coating. In [50], the specimens were slide burnished with base parameters  $r = 3$  mm,  $F_b = 300$  N,  $f = 0.05$  mm/rev and  $v = 100$  m/min, which are optimal under the “minimum roughness” criterion. It was found that with these basic parameters, the maximum fatigue limit ( $10^7$ -cycle fatigue strength) was achieved using six passes. The increase in the limit was 39.7%—from 340 to 475 Mpa. It was shown that a stabilized cycle of the surface layer was achieved with six passes, which is a necessary condition for maximizing the fatigue limit. In [40], it was found that SB of 42Cr4 steel with parameters  $r = 3$  mm,  $F_b = 225$  N,  $f = 0.1$  mm/rev and  $v = 100$  m/min increased the fatigue limit with 19.5%—from 410 to 490 MPa. Obviously, there is no information about the influence of the main parameters for the SB process on the fatigue limit of 41Cr4 steel.

In [43], it was established that in slide burnished specimens subjected to a rotating cyclic load, a fatigue macro-crack is formed at the boundary between the compressive zone and the bulk material. In other words, the roughness does not affect the fatigue behavior if compressive residual stresses are introduced at a significant depth from the surface layer and the surface residual stress is compressive. Therefore, in the present study, a combination of basic SB parameters will be sought, which, in combination, will result in a maximum depth of the compressive zone and maximum absolute value residual compressive stresses in 41Cr4 steel.

### 3 Theoretical background

The fully coupled thermal-stress FEM analysis procedure is used in order find the displacements/stresses simultaneously, on the one hand, and the temperature field when these two categories strongly influence each other, on the other. In matrix form, the coupled equations can be presented as follows:

$$\begin{bmatrix} K_{uu} & K_{uT} \\ K_{Tu} & K_{TT} \end{bmatrix} \begin{Bmatrix} \Delta u \\ \Delta T \end{Bmatrix} = \begin{Bmatrix} R_u \\ R_T \end{Bmatrix}, \tag{1}$$

where  $\Delta u$  and  $\Delta T$  are the respective corrections of the incremental displacement and temperature, the  $K_{ij}$  are

submatrices of the fully coupled Jacobian matrix, and  $R_u$  and  $R_T$  are, respectively, the mechanical and thermal residual vectors.

The heat transfer between the contacting surfaces of the diamond and the workpiece is defined as:

$$q_g = k(T_A - T_B), \tag{2}$$

where  $q_g$  is the heat flux density generated by the friction, passing from point  $A$  on one surface to a point  $B$  on the other surface;  $T_A$  and  $T_B$  are the temperatures of the two points; and  $k$  is the conductivity of the gap between the two surfaces.

The heat flux density generated by the friction is:

$$q_g = \eta \tau \dot{s} = \eta \tau \frac{\Delta s}{\Delta t}, \tag{3}$$

where  $0 < \eta \leq 1$  is a coefficient showing what proportion of the work done by friction dissipates into heat,  $\tau$  is stress from friction, and  $\Delta s$  and  $\Delta t$  are, respectively, increments of the slip and time.

For both contacting surfaces:

$$q_{g,i} = \varphi_i q_g, \quad i = 1, 2. \tag{4}$$

In the FEM simulations done in this study, it is assumed that  $\varphi_1 = \varphi_2 = 0.5$  and  $\eta = 1$ .

## 4 FE simulations

### 4.1 Material constitutive model

Although the material studied in the experimental part is 41Cr4 steel, in the FE simulations, the workpiece material is 37Cr4 steel since, for this material, a temperature-dependent constitutive model of the surface layers in the plastic field was obtained by us on the basis of temperature-dependent indentation tests, inverse FE analyses and developed methodology. Detailed information is given in [44]. This constitutive model gives the relationship between stress and strain tensors in the plastic field. During SB, each point within the surface under treatment is subjected to cyclic loading which provokes deformation anisotropy. Therefore, nonlinear kinematic strain hardening was used in the present study:

$$\dot{\alpha}_{ij} = \frac{C}{\sigma^0} (\sigma_{ij} - \alpha_{ij}) \dot{\epsilon}^{Pl} - \gamma \alpha_{ij} \dot{\epsilon}^{Pl} \tag{5}$$

where  $\alpha_{ij}$  is the back-stress tensor;  $C$  is the initial kinematic hardening modulus;  $\sigma^0$  is the equivalent stress defining the size of the yield surface, assuming that  $\sigma^0$  is valid for all possible stressed states and loading paths, and its initial magnitude at zero plastic strain is  $\sigma|_0$ ;  $\sigma_{ij}$  is the stress tensor;  $\gamma$  is the coefficient which determines the rate of decrease in

**Table 1** Temperature-dependent specific heat and conductivity for the workpiece portion [44]

$T, \text{ }^\circ\text{C}$	0	125	150	225	300	600
$c, \text{ J/kg }^\circ\text{C}$	473	563	585	655	675	750
$k, \text{ W/m}^2 \text{ }^\circ\text{C}$	54	51	49	47	45	38

**Table 2** Temperature-dependent specific heat and conductivity for the diamond deforming element [44]

$T, \text{ }^\circ\text{C}$	0	50	200	400	600
$c, \text{ J/kg }^\circ\text{C}$	420	600	1000	1500	1650
$k, \text{ W/m}^2 \text{ }^\circ\text{C}$	2500	2000	1400	1000	600

the kinematic modulus with increasing equivalent plastic deformation  $\bar{\epsilon}^{Pl}$ .

The temperature-dependent material characteristics  $C, \gamma,$  and  $\sigma|_0,$  as well as the Young’s modulus  $E$  and the coefficient of thermal expansion  $\alpha_t$  were obtained in [44]:

$$\begin{aligned}
 C &= -9 \times 10^{-5} T^3 + 0.0468 T^2 - 11.066 T + 12052, \text{ MPa} \\
 \gamma &= 3 \times 10^{-7} T^3 - 0.0002 T^2 + 0.0304 T + 36.238 \\
 \sigma|_0 &= -8 \times 10^{-6} T^3 + 0.0044 T^2 - 0.9599 T + 427.68, \text{ MPa} \\
 E &= (2.0196 - 0.00048 T) \times 10^5 \text{ MPa} \\
 \alpha_t &= (11.2 + 0.008 T) \times 10^{-6} \text{ m/m }^\circ\text{C}
 \end{aligned}
 \tag{6}$$

The above functions are defined in the temperature range  $T \in (0, 270 \text{ }^\circ\text{C})$ . The specific heat and conductivity (isotropic behavior) are temperature dependent and given in Table 1.

A purely elastic behavior is assumed for the deforming diamond element in SB. Young’s modulus is  $E = 10.5 \times 10^{11} \text{ Pa}$  and is assumed to be temperature independent. Poisson’s ratio is  $\nu = 0.1$ . The density and coefficient of thermal expansion are, respectively,  $\rho = 3515 \text{ kg/m}^3$  and  $\alpha_t = 1 \times 10^{-6} \text{ m/m }^\circ\text{C}$ . The specific heat  $c$  and the conductivity  $k$  with isotropic behavior are temperature dependent (Table 2).

### 4.2 FE models of SB process

A schematic diagram of SB process is depicted in Fig. 1. This scheme is the basis of the created FE models. In order to save time, two 3D fully coupled thermal-stress FE models were created in the present study. The first of these (two times fewer finite elements) was used to study the influence of the radius, burnishing force and burnishing velocity on the temperature generated and residual hoop stresses, whereas the feed rate was excluded from the model. It was assumed that the conclusions about the residual hoop stresses can be distributed on the residual axial stresses. The second model

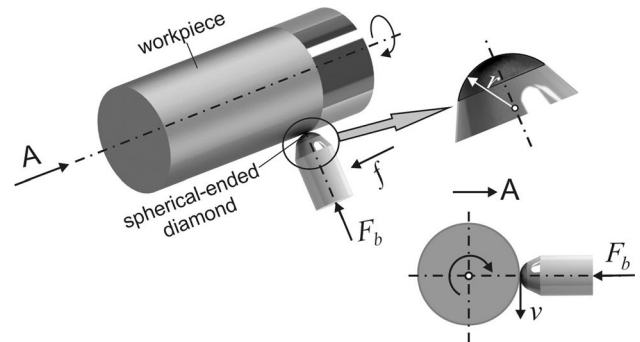


**Fig. 1** SB with spherical-ended deforming element

simulates the actual SB process with feed rate included, i.e., the relative motion of the deforming element tip relative to the surface being burnished is a screw line. The analysis time for the second model is about 40 h. The residual hoop and axial stresses obtained with this model (with SB parameters radius  $r = 3 \text{ mm}$ , burnishing force  $F_b = 300 \text{ N}$ , feed rate  $f = 0.07 \text{ mm}$  and burnishing velocity  $v = 80 \text{ m/min}$ ) were compared to measure stresses via the X-ray diffraction technique for a sample made of 37 Cr4 steel and slide burnished with the same parameters. Thus, the adequacy of the FE simulation was proven. The FE simulations were conducted by means of ABAQUS/Standard. The version of ABAQUS used allows a fully coupled thermal-stress analysis to be conducted using nonlinear kinematic strain hardening.

Figure 2 shows the first FE model. The feed rate has not been taken into account. For this reason, the advantage of symmetry was used—only half of the portion to be modeled for the “deforming element—workpiece” system was modeled. The previous treatment of the workpiece cylindrical surface via cutting used a feed rate of  $f_c = 0.1 \text{ mm/rev}$ . The initial kinematic roughness was modeled in order to achieve a more realistic representation of the workpiece geometry. From the workpiece, starting at the cylindrical surface, a body with the approximate size  $5 \times 4 \times 4 \text{ mm}$  was selected by two concentric cylindrical surfaces and two pairs of planes. On the three free faces of the workpiece portion, an “elastic foundation” contact was defined with a coefficient numerically equal to Young’s modulus. Thus, the interaction of the modeled portion with the rest of the workpiece was taken into account. Two types of contacts were defined between the deforming elements and the workpiece portion: mechanical—a normal and tangential contact with friction, and thermal—heat generation from friction with

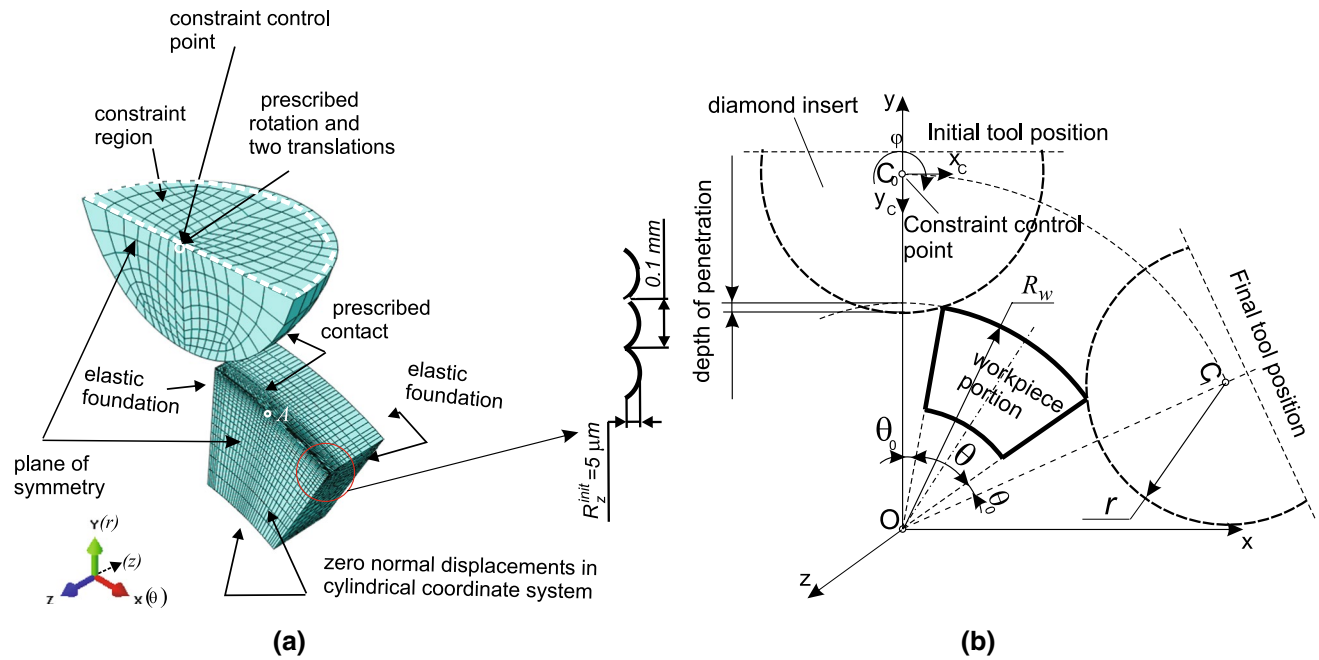


Fig. 2 First 3D fully coupled thermal-stress FE model: a general view; b scheme for determination of the kinematics

coefficients  $\eta = 1$  and  $\varphi_1 = \varphi_2 = 0.5$ . The friction coefficient  $\mu$  was assigned in accordance with Maximov et al. [52]. Figure 3 shows the dependence of the friction coefficient on the radius, burnishing force, feed rate and burnishing velocity, according to [52]. Heat transfer was assigned between the contacting surfaces, with heat transfer coefficients changing according to a linear law describing the clearance between

them: conductivity = 50 W/m<sup>2</sup> °C at clearance = 0 and conductivity = 0 at clearance = 0.0001 m. Due to the very short duration of the modeled process, convection and radiation were ignored. On the plane of symmetry of the workpiece portion, as well as on the inner cylindrical surface, zero normal displacements were assigned in a cylindrical

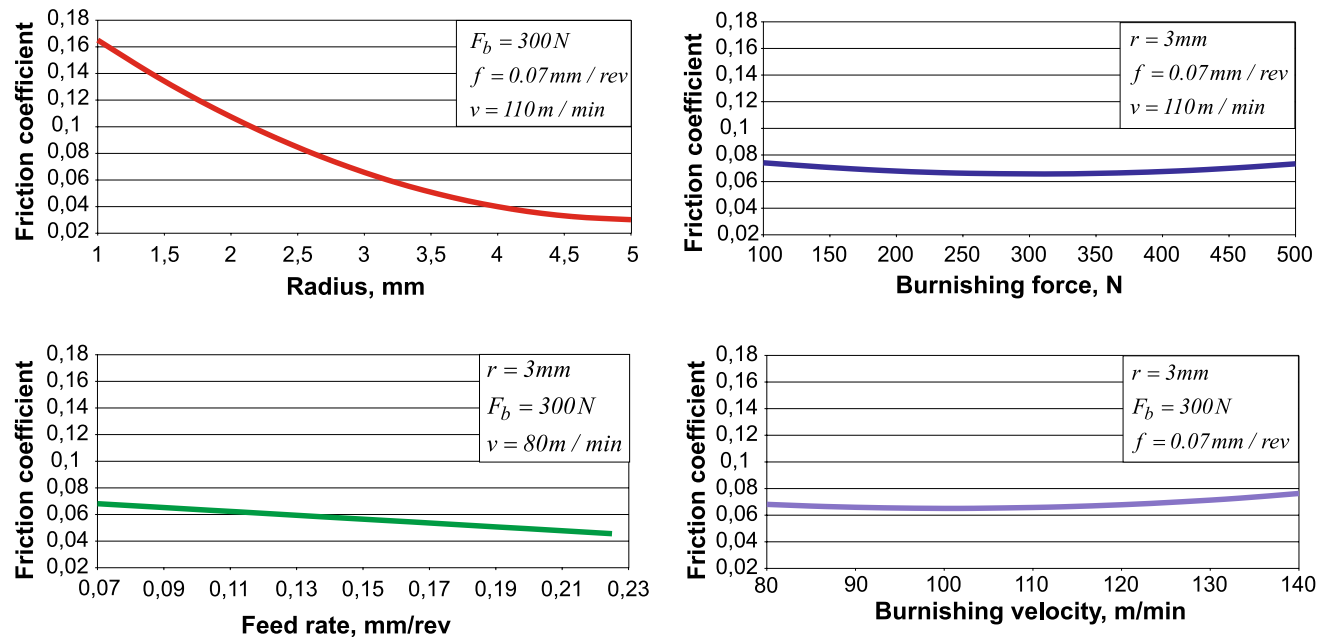


Fig. 3 Dependence of the friction coefficient on the SB parameters

coordinate system. The deforming element motion with respect to the fixed workpiece portion was defined as one rotation, and two translations were assigned to the so-called constraint control point. Thus, the deforming diamond slides over the workpiece cylindrical surface. The trajectories of the constraint control points are central circles. Therefore, the two translations of this control point, respectively, along the  $x$  and  $y$  axes are matched in real time. For this purpose, periodic time curves were used. The assigned displacements of the constraint control point of the deforming element, in accordance with the indications in Fig. 2, are the following:

$$\varphi = \theta + 2\theta_0, \tag{7}$$

where

$$\theta_0 \geq \arccos \frac{R_w^2 - r^2 + (R_w + r - d_p)^2}{2R_w(R_w + r - d_p)}, \tag{8}$$

$$x_C = B \sin \omega t, \quad y_C = -A + A \cos \omega t \tag{9}$$

where

$$A = B = R_w + r - d_p, \tag{10}$$

$$\omega = \frac{\theta + 2\theta_0}{t^*}, \tag{11}$$

$$t^* = \frac{R_w(\theta + 2\theta_0)}{v}, \tag{12}$$

$v$ , m/s is burnishing velocity. The international system of units was used for the components in the above equations.

The burnishing force was set in accordance with the deforming element depth of penetration. Their interdependence was established by a preliminary FE analysis (Fig. 4). Since the burnishing creates a very high gradient of the strains in the normal direction (with respect to the surface layer), a very fine mesh near the surface was used.

The modeled portion of the workpiece was discretized with 9928 coupled temperature-displacement FEs: 9622 linear hexahedral elements of type C3D8T and 306 linear wedge elements of type C3D6T. The total number of nodes was 11,550.

The second FE model is shown in Fig. 5. The model includes the influence of the feed rate: therefore, symmetry cannot be used, i.e., the model contains two times more finite elements compared to the simplified model in Fig. 2. The basic parameters of the SB process are: radius  $r = 3$  mm, burnishing force  $F_b = 300$  N and burnishing velocity  $v = 80$  m/min. Three simulations were conducted with a feed rates of  $f = 0.07$  mm/rev,  $f = 0.1$  mm/rev and  $f = 0.13$  mm/rev. The selected feed rate interval is consistent with [52] in order to assign the friction coefficient

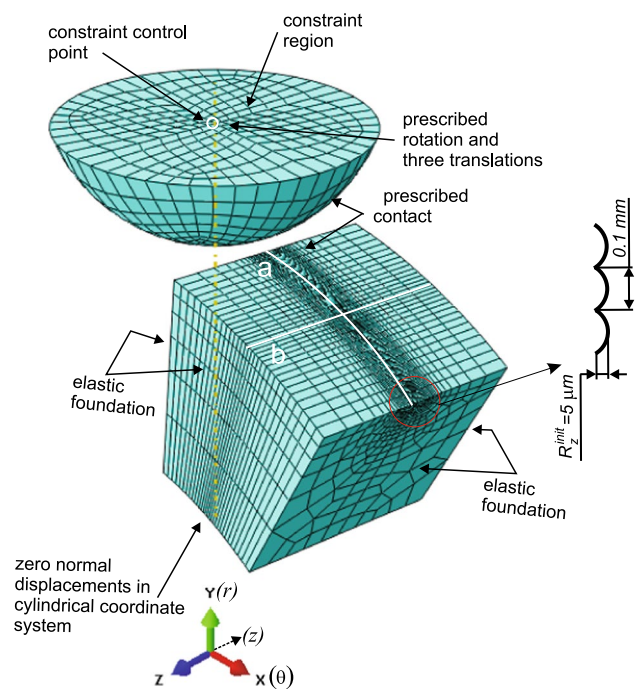
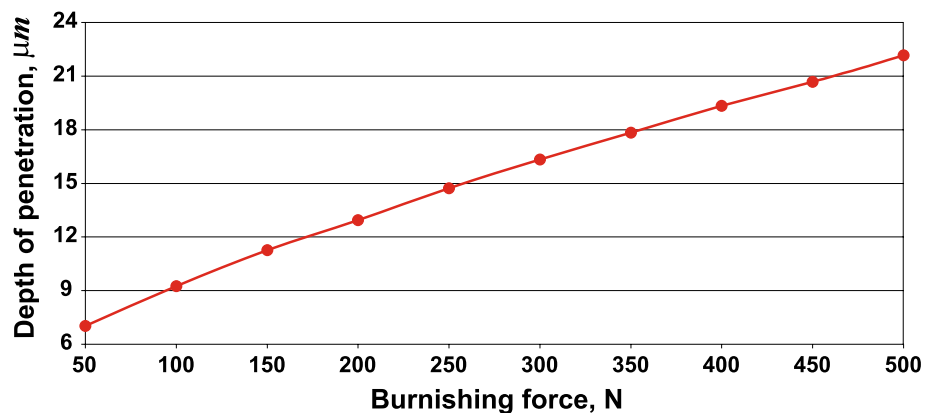


Fig. 5 Second 3D fully coupled thermal-stress FE model

Fig. 4 Interdependence between the burnishing force and the depth of penetration



values accurately. According to [52], the friction coefficients between the diamond and the surface being burnished are, respectively,  $\mu = 0.0681$ ,  $\mu = 0.0638$  and  $\mu = 0.0594$ . The trajectory of the deforming element tip relative to the workpiece portion is a screw line with a pitch equal to the feed rate size. In order to assign the screw movement of the deforming element, three translations on the three axes, respectively, and one rotation around the  $z$  axis are assigned to the constraint control point of the deforming element. Displacements along the  $x$  and  $y$  axes are defined by two periodic time curves, according to Eq. (9). The deforming element makes a total of 10 revolutions around the  $z$  axis (i.e., workpiece axis), whereby the displacement along the same  $z$  axis is  $Z = 10f$ . The initial position of the deforming element is selected so that this displacement will be symmetric relative to the arc  $a$  (see Fig. 5). The total real time is  $T^* = \frac{20\pi R_w}{v}$ .

The resulting residual stress distribution was considered at the nodes lying on the intersection of the two planes of symmetry (defined by the arc  $a$  and the generatrix  $b$  in Fig. 5) of the modeled portion of the workpiece.

## 5 FE results and discussion

### 5.1 Parametric study

The heat generated is a consequence of just the sliding friction between the deforming diamond and the surface being treated, according to Sect. 3. In the present study, the heat due to plastic deformation work is not taken into account since the friction force work is significantly larger than the plastic deformation work. Comparison between the two works obtained by preliminary QE analysis is depicted in Fig. 6. The neglect of heat due to surface plastic deformation work partially reduces the thermal effect. On the other hand, the ignoring of the other two forms of heat transfer (convection and radiation) in the FE analyses partially offsets the inaccuracy introduced. Therefore, reliable information regarding the friction coefficient is crucial to the accuracy of the results obtained. In [52], extensive research on, and modeling of, the friction coefficient was carried out depending on the radius  $r$ , burnishing force  $F_b$ , feed rate  $f$  and burnishing velocity  $v$  in the SB of 42Cr4 steel using a polycrystalline diamond. The results obtained for the coefficient of friction are used in the present study. Therefore, in this study, the variation intervals for the four main parameters for the SB process are the same as in [52]. Since the first FE model (see Fig. 2) is simplified (the feed rate is ignored; only one displacement of the deforming element is modeled in a circumferential direction in the plane of symmetry of the workpiece modeled portion), the results obtained for the residual hoop stresses are representative only in a qualitative

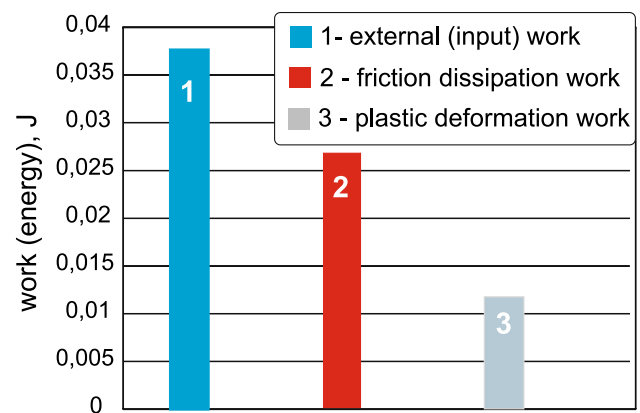


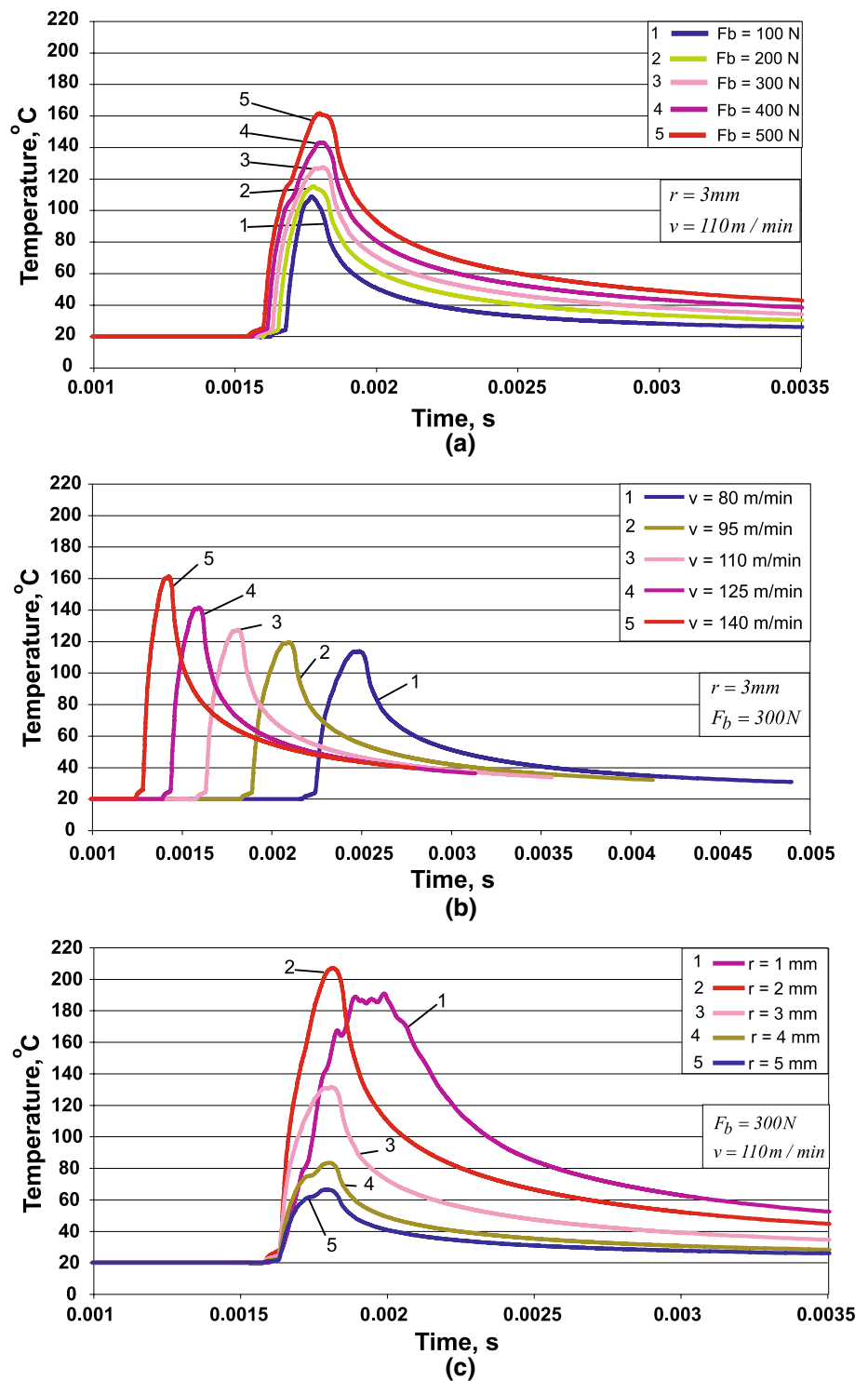
Fig. 6 Comparison between friction and plastic deformation work

aspect. However, these results enable a qualitative assessment of the impact of the three parameters  $r$ ,  $F_b$  and  $v$  on these stresses.

Figure 7 shows a change in the temperature at point  $A$  (see Fig. 2) as a function of time. This point on the surface being treated belongs simultaneously to the two planes of symmetry of the modeled portion. Figure 6a examines changing the temperature for different values of the burnishing force, while the radius and burnishing velocity are held constant. The maximum temperature increases progressively (at an increasing rate) with increasing burnishing force. The friction coefficient (see Fig. 3) is very slightly affected by the burnishing force. Since the velocity is constant, the temperature peak is due only to the increase in the tangential stress  $\tau$  (see Eq. 3), due to the increased burnishing force. As a result, the heat flow density  $q_g$  increases; hence, the temperature increases. Figure 6b shows the alteration of the temperature for different burnishing velocities when the radius and burnishing force are held constant. As the velocity increases, the maximum temperature increases exponentially. The reason for this relationship is the following. The heat flow density  $q_g$  increases linearly with increasing velocity. Simultaneously, the tangential friction stress  $\tau$  changes as the friction coefficient changes (see Fig. 3). In the interval  $80 \leq v < 100$  m/min, the friction coefficient decreases, and, when  $v = 100$  m/min, this coefficient hits a minimum and then increases. The tangential stress  $\tau$  follows the same trend. According to Eq. (3), the heat flow density increases at an increasing rate, which explains the exponential rise in the temperature at point  $A$ . Figure 6c shows the variation in the temperature for different radii when the burnishing force  $F_b$  and burnishing velocity  $v$  are constant. Decreasing the radius to  $r = 2$  mm results in the maximum temperature at point  $A$  increasing exponentially. Although  $F_b$  and  $v$  are constant, the friction coefficient increases rapidly with decreasing radius (see Fig. 3). As a result, the tangential stress  $\tau$  grows strongly, as does the heat flow density (see



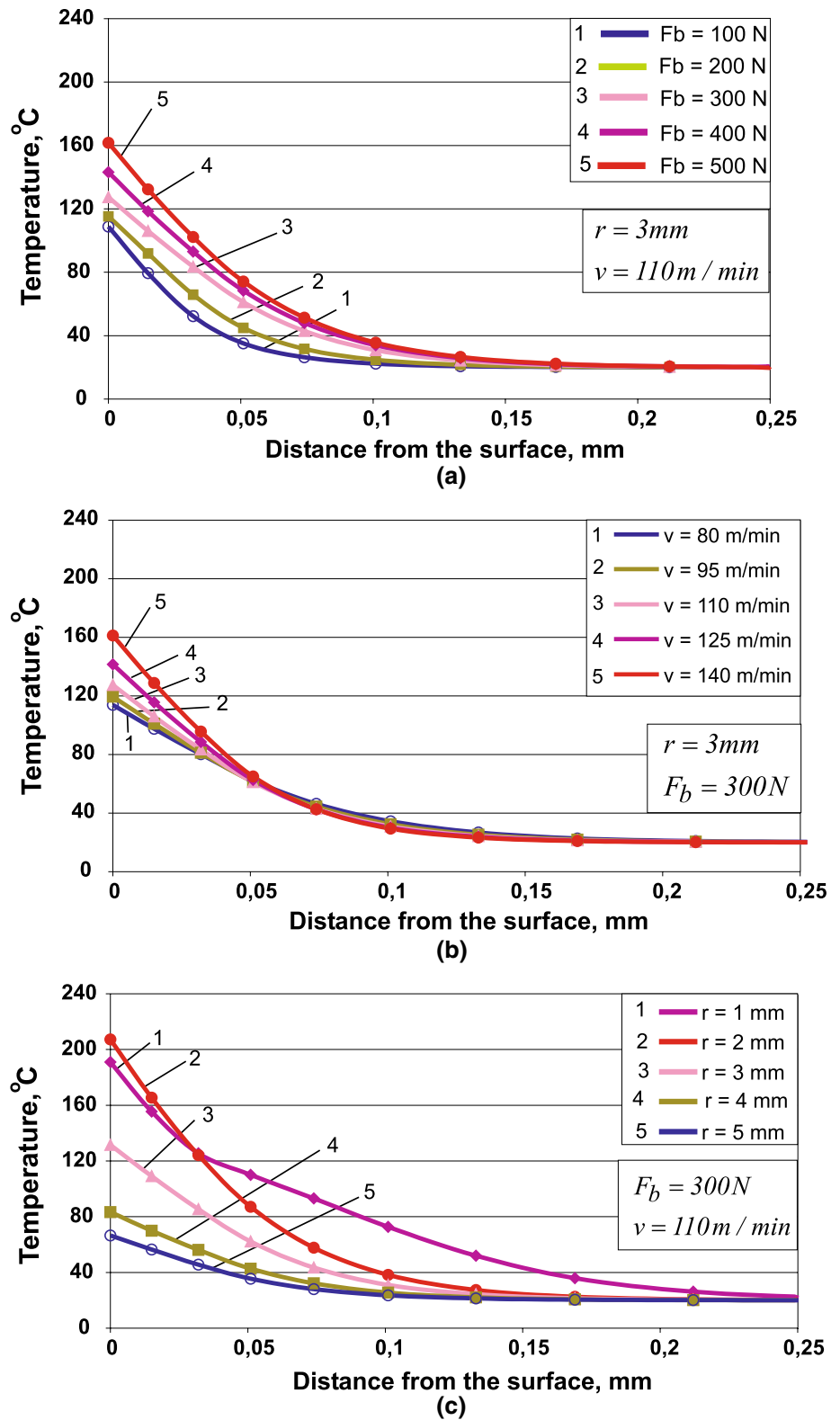
**Fig. 7** Change in the temperature at point A as a function of the time: **a** at different burnishing forces; **b** at different burnishing velocities; **c** at different radii



Eq. 3). The trend changes when  $r = 1\text{ mm}$ . The maximum temperature is smaller compared to the case when  $r = 2\text{ mm}$ , but it keeps its magnitude considerably longer. The following explanation can be given. When  $r = 1\text{ mm}$ , the area of the contact spot between the deforming element and the surface being treated decreases drastically. However, the temperature gradient on the surface and in the depth in the

vicinity of point A is greatest; as a consequence, the conductive heat transfer intensifies significantly both on the surface and in depth in the direction of the neighboring regions with lower temperatures. This explanation is confirmed by Fig. 8, which shows the temperature distribution at a depth from the surface, starting from point A, at the moment in which the temperature at point A is at a maximum. The minimum

**Fig. 8** Temperature distribution in a depth from the surface, starting from point A: **a** at different burnishing forces; **b** at different burnishing velocities; **c** at different radii

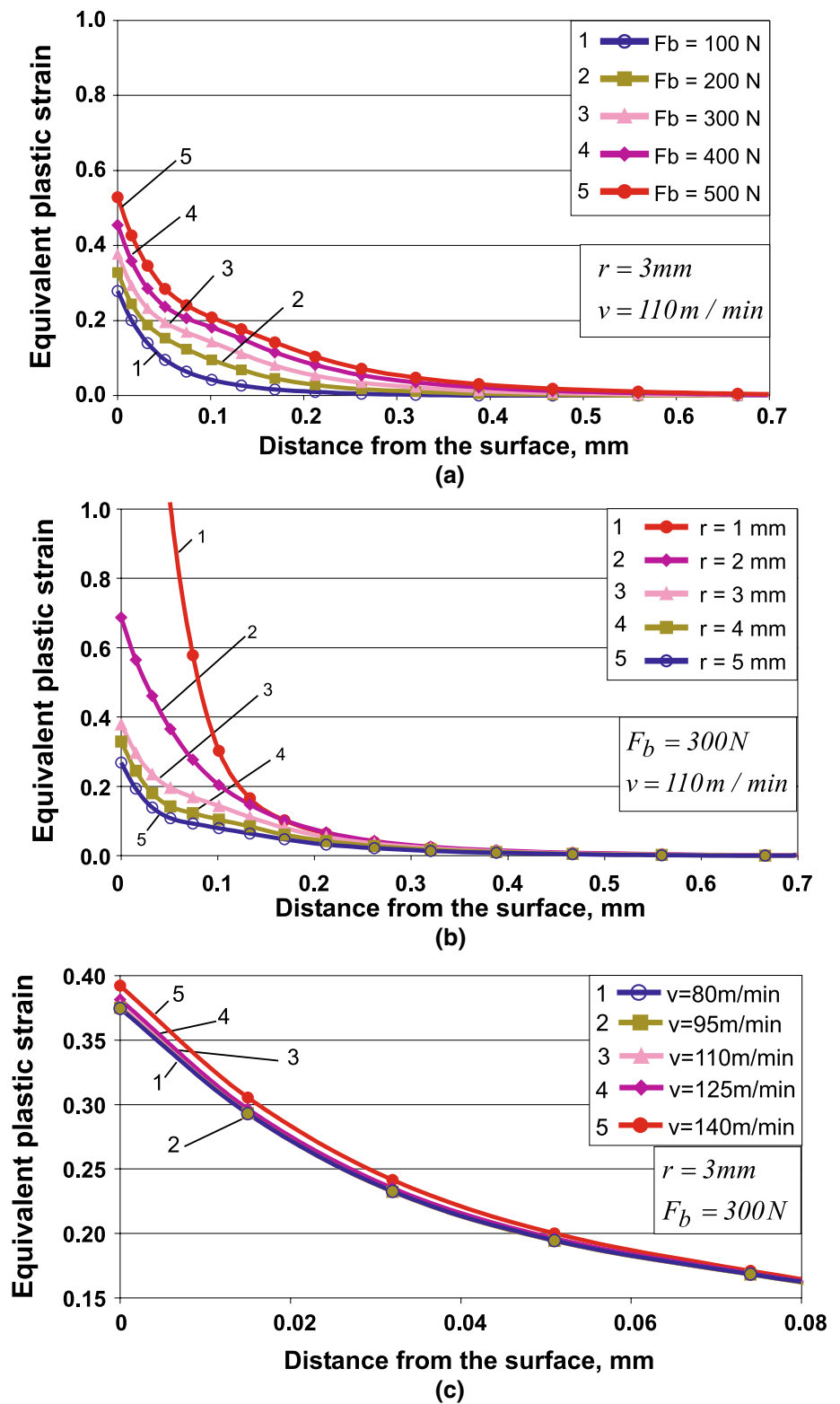


radius (see Fig. 8c) provides the maximum depth at which the temperature has practical significance.

Figure 9 shows the equivalent plastic strain distribution at a depth from the surface, starting from point A.

This deformation and its gradient are greatest on the surface and decrease rapidly with depth. Taking Fig. 8 into account (the case in which the temperature is at a maximum on the surface and decreases rapidly with

**Fig. 9** Equivalent plastic strain distribution: **a** at different burnishing forces; **b** at different radii; **c** at different burnishing velocities



depth, such as after about 0.1 mm is without practical importance), the maximum gradient of the equivalent plastic strain on the surface can be explained by the presence of thermoplastic components. As can be expected,

increasing the burnishing force (Fig. 9a) increases the strain and this increase is most significant on the surface. The influence of the burnishing force manifests itself tangibly to a depth of 0.4 mm, then becomes negligible.

Of the three parameters, the radius exerts the strongest influence on the equivalent plastic strain, and this effect is significant to a depth of 0.12 mm (Fig. 9b). Obviously, the combination of minimum radius and greater force results in an excessively large plastic deformation. In this case, it can be predicted that multiple micro-defects (local destruction) will accumulate in the surface layer. Therefore, the minimum radius ( $r = 1$  mm) is excluded in the experimental studies in Sect. 6. Figure 9c confirms that the burnishing velocity affects the equivalent plastic strain the least. Apparently, the increase in the burnishing velocity in the investigated range leads to a slight increase in the equivalent plastic strain. Since the constitutive model is rate independent, this surface effect is due only to the increase in the thermoplastic component, as a consequence of the large temperature gradient.

The effect of the three parameters on the residual hoop stress distribution in depth, starting from point A, is shown in Fig. 9. The change in the burnishing force results in relatively less variation in residual stresses on the surface but, in a significant change, in depth from the surface (Fig. 10a). The increase in the burnishing force does not change the maximum absolute value of the residual stress but results in a three-fold increase in the compressive field depth (for  $F_b = 100$  N, the depth of the compressive zone is about 0.25 mm, while for  $F_b = 500$  N, the depth is about 0.75 mm). As could be expected, the change in the radius changes the distribution law of the residual hoop stresses significantly (Fig. 10b). At the same time, a clear trend in the distribution is not observed when the radius increases. The reason for this result is the complex influence of the mechanical and temperature factors. As a whole, when the radius increases, the maximum absolute values of the residual stresses increase and the depth of the compressive zone remains constant—about 0.75 mm. Smaller radii lead to greater friction coefficients (see Fig. 3), respectively, for the residual stress relaxation in the surface layer due to the larger amount of generated heat. Figure 10c shows the influence of the burnishing velocity on the residual hoop stress distribution. Since the material constitutive model is rate independent, the figure illustrates only the influence of the temperature factor. Due to the heat generated, residual stress relaxation is observed on the surface. With an increase in the burnishing velocity, this effect increases, and, at  $v = 140$  m/min zero values of the residual stresses are observed at a depth of approximately  $0.04 \div 0.05$  mm. In other words, a tendency is observed for the appearance of a narrow zone with tensile residual stresses if the burnishing velocity increases above 140 m/min. This effect is highly undesirable since the bending stresses are greatest in the surface layer and the probability of the formation of fatigue macro-cracks on

the surface is large. Therefore, it is advisable that the burnishing velocity not exceed  $v = 100$  m/min.

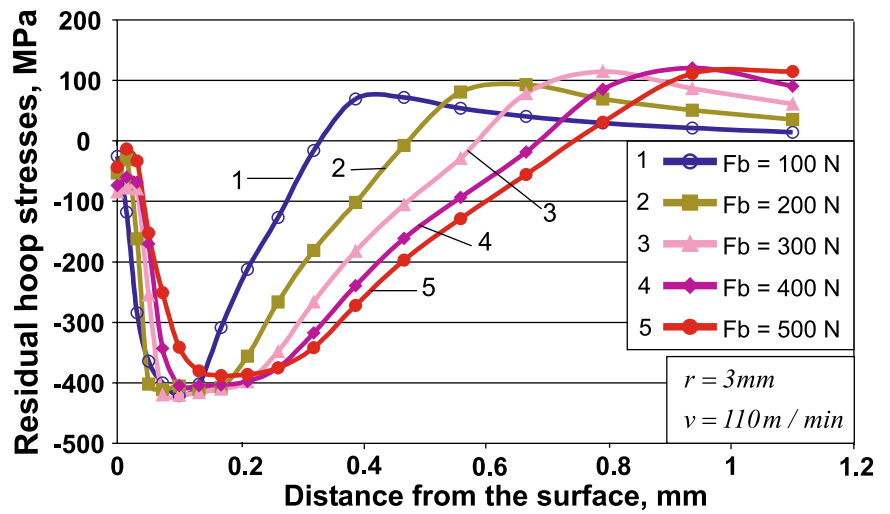
## 5.2 Effect of the feed rate on the residual stresses

Residual stress distributions for different feed rates are depicted in Fig. 11. Evidently, the influence of the feed rate is less pronounced than the influences of the radius and burnishing force. For both stresses, the change in the residual stress distribution depending on the feed rate shows one and the same trend. The surface residual stresses decrease as the feed rate increases. At a depth of 0.01 mm for the hoop stresses, respectively, 0.03 mm for the axial stresses, the trend changes drastically. After a depth of 0.12 mm for the hoop stresses, respectively, 0.3 mm for the axial stresses, the feed rate (in the investigated range) practically does not affect the residual stresses. It is important to note that the depth of the compressive zone for both stresses remains virtually one and the same.

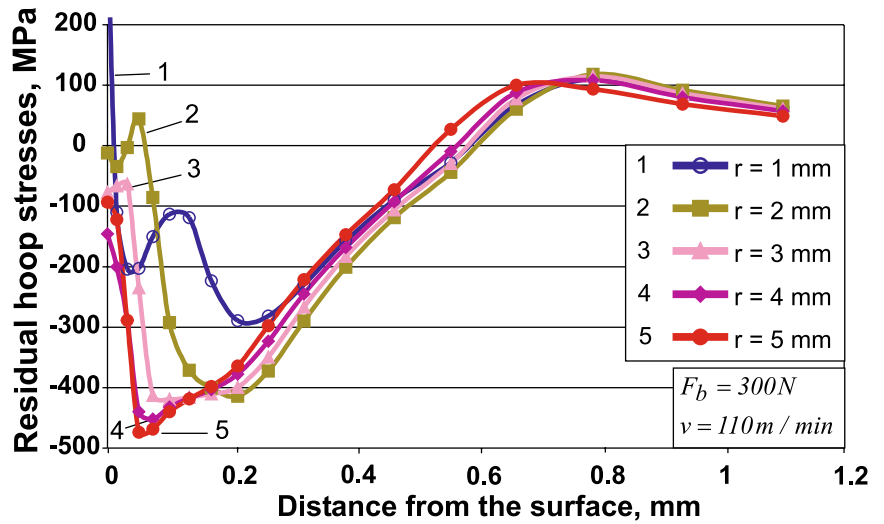
## 5.3 Verification of FE model adequacy

The adequacy of the FE models was evaluated by comparing the FE results for the residual stresses with experimental results. A cylindrical specimen with a diameter of 22 mm was subjected to SB using a polycrystalline diamond with a spherical end on a CNC T200 lathe. The SB parameters were: radius  $r = 3$  mm, burnishing force  $F_b = 300$  N, feed rate  $f = 0.07$  mm/rev and burnishing velocity  $v = 80$  m/min. These SB parameters were used in the FE model as shown in Fig. 5. The specimen was produced through a technology which removes (at least partially) all residual stresses except those introduced by precision turning, as follow: turning, heat treatment—annealing at 550 °C for 2.5 h, precision turning and burnishing. The specimen was clamped on one side with the chuck and supported on the other side. Precision turning and burnishing were carried out in one clamping process to minimize the concentric run-out in burnishing. A DNMG 50608 RF carbide cutting insert was used for the precision turning. The initial roughness (before burnishing) was  $R_a = 1.25$  μm. The residual axial stress distribution at depth from the surface was found using the X-ray diffraction technique. In order to analyze the stress gradient under the specimen's surface, the material layers were removed gradually via electrolytic polishing. The measurement was conducted by Professor Nick Ganey at the Czech Technical University in Prague. Figure 12 shows the comparison between the FE and X-ray diffraction results. Obviously, there is good agreement between the FE simulations and the experiment. Thus, FE model adequacy is proven.

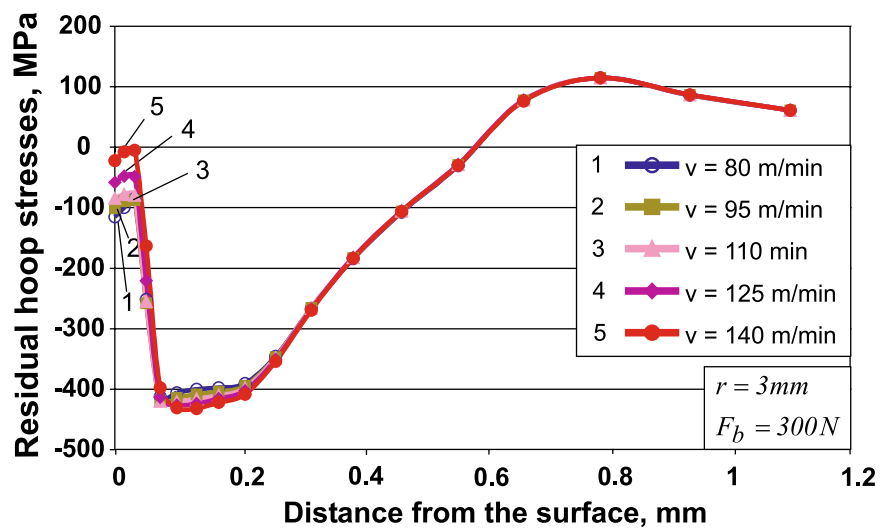
**Fig. 10** Residual hoop stress distribution: **a** at different burnishing forces; **b** at different radii; **c** at different burnishing velocities



(a)



(b)



(c)

**Fig. 11** Residual stress distributions for different feed rates

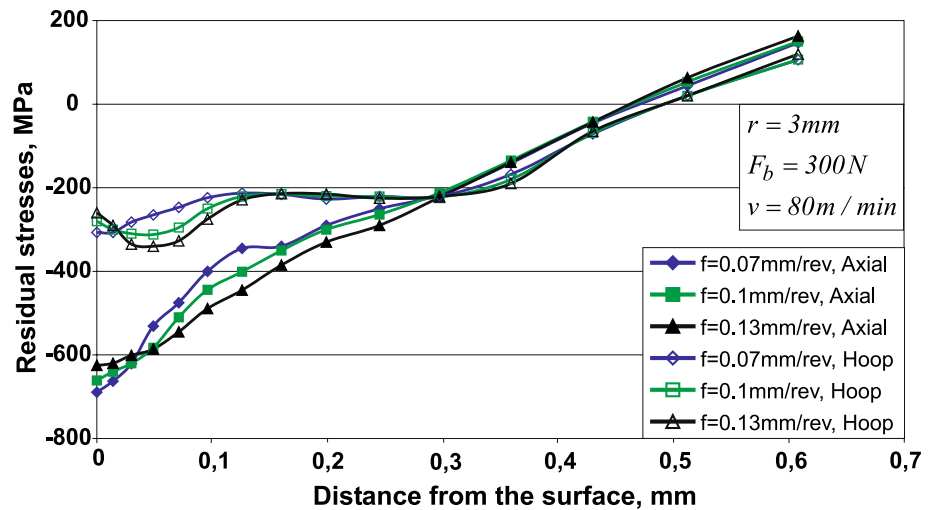
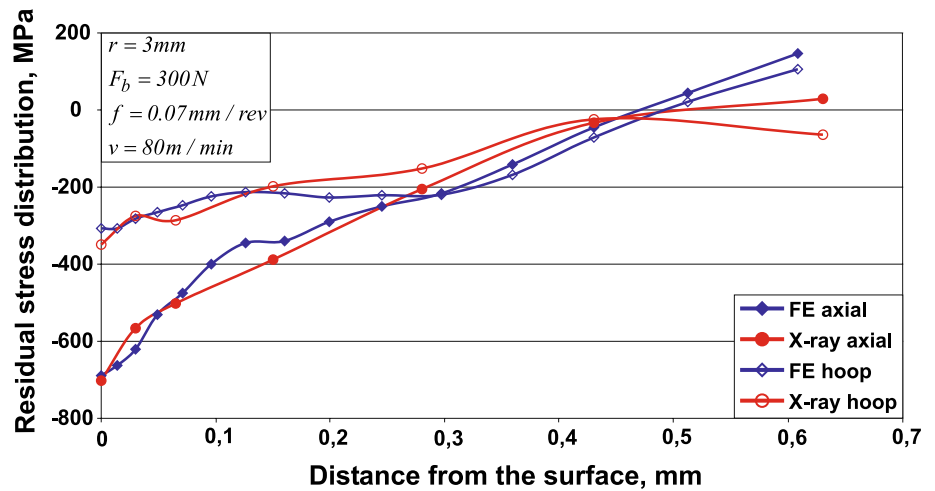


**Fig. 12** Comparison between FE and X-ray diffraction results for the residual stresses



## 6 Experiment

### 6.1 Purpose of the experiment

FE simulations show that the diamond radius and burnishing force have the strongest effects on the residual stresses. These stresses, in turn, have a significant influence on the fatigue strength, respectively, fatigue life. Therefore, the aim of the experiment was to evaluate the influence of these two parameters on the fatigue strength of samples subjected to SB.

### 6.2 Locatti's method

In addition to Wöhler's method, there are a large number of methods which can be used to study the fatigue behavior of specimens. They can be divided into two main groups: (1)

methods for examining the incline on the Wöhler's curve (including low-cycle fatigue behavior); and (2) methods for determining the fatigue limit. As the majority of structural and machine components work under relatively low loads, the second set of methods is essential. This group includes two subgroups: (a) methods of long duration (the "probit" method; Dixon–Mood's method; Robbins–Monro's method; Freundenthal's method and others); (b) accelerated methods (the Pro-Nedeshan's method; temperature method; electrical resistance method; energy dissipation method; Locatti's method and others). Of all the accelerated methods for determining the fatigue limit, Locatti's method provides the best approximation to Wöhler's method. Locatti's method is based on the Palmgren–Miner linear damage hypothesis, which is a particular case of a general cumulative damage theory [53]. A single specimen is needed. The specimen is subjected to stepwise increasing stress amplitudes with a constant step. Here, the initial stress amplitude is smaller than the assumed

fatigue limit and the number of cycles  $n_i$  is one and the same for each stress amplitude. The loading is increased until the specimen is destroyed. In order to determine the number of cycles to failure  $N_i$  for each stress amplitude  $\sigma_{a,i}$ , it is alleged that Wöhler’s curve must be constructed. It is appropriate to choose at least three alleged values of the fatigue limit, i.e., at least three Wöhler’s curves must be constructed. For each curve, the sum of the accumulated damages is calculated as:  $\sum_{i=1}^{\bar{k}} (n_i/N_i)$ , where  $\bar{k}$  is the number of stress amplitudes. The stress, obtained by interpolating for  $\sum_{i=1}^{\bar{k}} (n_i/N_i) = 1$ , is the fatigue limit.

In the present study, Locatti’s method was used to find the fatigue limits of samples subjected to SB with different combinations of process parameters. For each combination of radius and burnishing force, three samples were used. Thus, the fatigue limit  $\sigma_{-1}$  for each combination (each experimental point) is obtained as an arithmetic mean of the results for the three samples.

### 6.3 Conditions of the experiment

#### 6.3.1 Material

The material used in the experiment was 41Cr4 medium-carbon low-alloy steel with chemical composition as follows: C-0.41 wt%, Si-0.25 wt%, Mn-0.71 wt%, Cr-0.93 wt%, P-0.012 wt%, S-0.012 wt%, Cu-0.28 wt%, Ni-0.09 wt%, Al-0.024 wt%, Ti-0.022 wt%, Mo-0.015 wt%, N-0.01 wt%, Fe-balance. The average mechanical characteristics of this batch of 41Cr4 steel was established in our “Testing of Metals” laboratory: Young’s modulus  $E = 2 \times 10^5$  MPa; yield limit  $\sigma|_0 = 789$  MPa; ultimate stress  $\sigma_u = 986$  MPa; elongation  $A_5 = 10.3\%$ ; and transverse contraction  $z_t = 26\%$ . The stress–strain curves, as well as Wöhler’s curve, for this steel

(obtained by us) are shown in Fig. 13. The fatigue limit is  $\sigma_{-1} = 440$  MPa.

#### 6.3.2 Experimental design

A planned experiment was carried out. FE simulations show that the residual stresses are most affected by the diamond radius  $r$  and burnishing force  $F_b$ . Therefore, these two parameters were chosen to be governed. The levels of these SB parameters are depicted in Table 3. The impact of the feed rate on the residual stresses is less than those of these two parameters. Given the residual stress distribution in Fig. 11, a feed rate of 0.05 mm/rev was chosen. Based on the outcomes from the parametric study, the burnishing velocity was chosen to be  $v = 100$  m/min. Table 4 contains the experimental design.

#### 6.3.3 Specimens and conditions of the experiment

Hourglass-shaped specimens (Fig. 14) with minimum diameters of 7.5 mm were prepared on a CNC T200 lathe. The specimens were slide burnished with a constant feed rate and burnishing velocity, respectively,  $f = 0.05$  mm/rev and

**Table 3** Governing factors and their levels

Governing factors	Levels of the factors			
	Coded			
	-1	-0.333	+0.333	+1
Naturals $\bar{x}_i$	Coded $x_i$	Natural		
Diamond $r$ [mm], $\bar{x}_1$	$x_1$	2	3	4
Burnishing force $F_b$ [N], $\bar{x}_2$	$x_2$	100	200	300
		400		

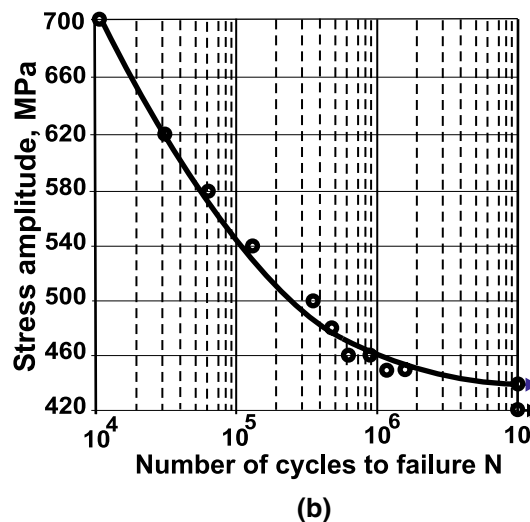
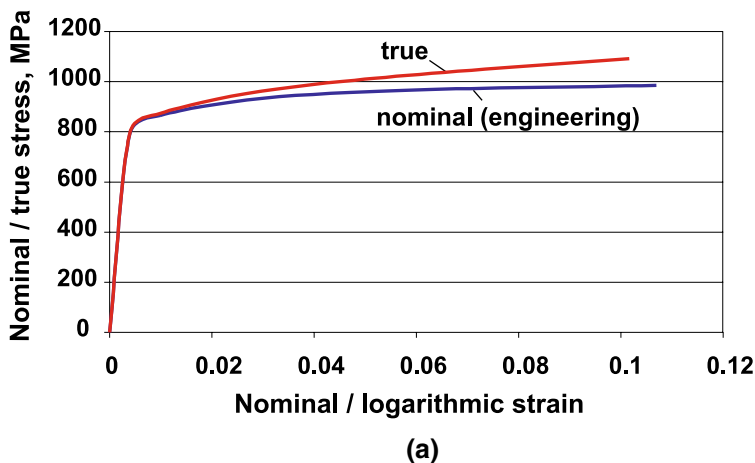


**Fig. 13** Mechanical characteristics of 41Cr4 steel: **a** stress–strain curves; **b** Wöhler’s curve

**Table 4** Experimental design

No.	$r, x_1$	$F_b, x_2$	Experiment				Model	Error%
			$\sigma_{-1}^{(1)}, \text{MPa}$	$\sigma_{-1}^{(2)}, \text{MPa}$	$\sigma_{-1}^{(3)}, \text{MPa}$	$\sigma_{-1}, \text{MPa}$	$\bar{\sigma}_{-1}, \text{MPa}$	
1	-1	-1	495.0	495.4	488.1	492.83	494.38	0.3145
2	+1	-1	489.4	482.8	479.1	483.77	484.41	0.1323
3	-1	+1	537.1	514.5	528.0	526.53	525.56	-0.1842
4	+1	+1	514.0	533.7	523.9	523.80	528.17	0.8343
5	-1	-0.333	505.1	524.8	506.9	512.27	510.11	-0.4216
6	-1	+0.333	516.0	528.9	522.2	522.37	523.94	0.3006
7	+1	-0.333	498.4	493.5	499.4	497.10	498.20	0.2213
8	+1	+0.333	504.0	532.5	530.4	522.30	516.22	-1.1641
9	-0.333	-1	489.9	497.3	483.8	490.33	491.12	0.1611
10	+0.333	-1	452.9	459.7	474.7	462.43	459.43	-0.6487
11	-0.333	+1	537.5	530.3	526.3	531.37	534.38	0.5665
12	+0.333	+1	508.1	518.8	512.9	513.26	506.89	-1.2411
13	-0.333	-0.333	515.4	517.4	506.7	513.17	508.83	-0.8457
14	+0.333	-0.333	474.3	469.1	470.0	471.13	476.50	1.1398
15	-0.333	+0.333	523.7	529.9	524.9	526.17	526.69	0.0281
16	+0.333	+0.333	488.4	483.6	503.3	491.77	495.75	0.8093

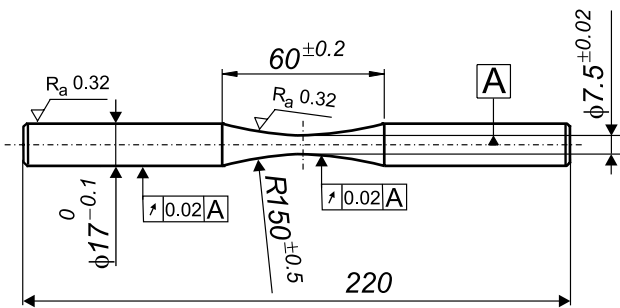


**Fig. 14** Hourglass shaped fatigue specimen

$v = 100$  m/min, but with different combinations of diamond radii and burnishing forces. Polycrystalline diamond inserts were used as the deforming elements in the SB process in the presence of the lubricant Hacut 795-H. Bending fatigue tests were conducted on an MUI-6000 electromechanical testing machine under the conditions of load control and rotating-bending loading with a cycle asymmetry factor  $R = -1$ . The loading frequency was 100 Hz in air.

**6.3.4 Details of Locatti’s method**

The alleged Wöhler’s curves and the stepwise increasing stress amplitude are shown in a double logarithmic coordinate system in Fig. 15. The basic curve (the central curve of the figure) was obtained in [40] for 42Cr4 steel, as the samples have been processed by SB with the following parameters:  $r = 3$  mm,  $F_b = 225$  N,  $f = 0.1$  mm/rev and  $v = 100$  m/min. The fatigue limit is  $\sigma_{-1} = 490$  MPa. The

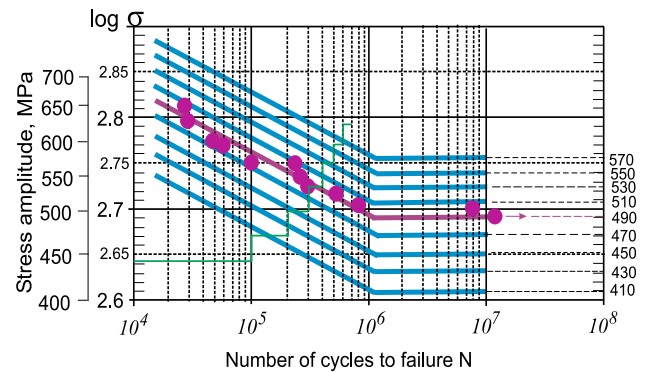


**Fig. 15** Experimental and alleged Wöhler’s curves and stepwise increasing stress amplitude in double logarithmic coordinate system

other eight curves are arranged two-by-two in parallel with the basic curve, as the fatigue limit changes from 410 to 570 MPa in the 20 MPa step. The stepwise increasing stress amplitude starts at 440 MPa and increases in steps of 30 MPa. For each step, the base number of cycles is  $n_i = 10^5$  (the step at which the sample is destroyed is an exception).

**6.4 Experimental results**

Table 4 shows the results obtained for the fatigue limits. In this study, a regression analysis of the experimental results was carried out using QstatLab software [54]. The regression model was chosen to be a polynomial of degree no



greater than three since the governing factors are changed at four levels. In order to carry out a proper statistical analysis, the coefficients in the polynomial should number no more than 16 (which is the number of the experimental points). The following model was obtained for the fatigue limit:

$$\begin{aligned} \sigma_{-1} = & 501.177 - 53.1935x_1 + 28.989x_2 + 11.443x_1^2 \\ & - 4.486x_2^2 + 47.904x_1^3 - 5.817x_2^3 + 3.143x_1x_2 \\ & - 4.439x_1^2x_2 + 3.451x_1x_2^2 \end{aligned} \quad (13)$$

The maximum deviation (relative error) of the model compared to the experimental results is less than 1.25% (see Table 4). A graphical visualization of the model obtained (13) is shown in Fig. 16. As can be seen, for all radii, the increase in the burnishing force leads to an increase in the fatigue limit, which can be explained by the increased depth of the compressive zone (see Fig. 10a). The influence of the radius is more complex and cannot be explained by the residual stresses alone. The explanation should be sought in the favorable combination of micro- (modified microstructure) and macro- (beneficial residual stresses) effects. It is necessary to find the maximum fatigue limit predicted by Eq. (13). A one-purpose optimization was conducted using QstatLab’s genetic algorithm [54]. The optimal values of the governing factors are  $x_1^{opt} = -0.6311$  (respectively,  $r = 2.553$  mm) and  $x_2^{opt} = 0.8803$  (respectively,  $F_b = 382$  N), providing the fatigue limit  $\sigma_{-1} = 540.35$  MPa. The radii of the diamonds produced, however, are discrete numbers—they change with a pitch of 0.5 mm. Hence, Fig. 17 shows sections of the surface of the fatigue limit (in natural coordinates) with planes  $r_i = \text{const}$ . Obviously, the radius  $r = 2.5$  mm, in combination with burnishing force  $F_b = 380$  N, ensures the fatigue limit  $\sigma_{-1} \approx 540$  MPa. Therefore, the optimal SB parameters under the “maximum fatigue limit” criterion are:  $r = 2.5$  mm,  $F_b = 380$  N,  $f = 0.05$  mm/rev and  $v = 100$  m/min. After the

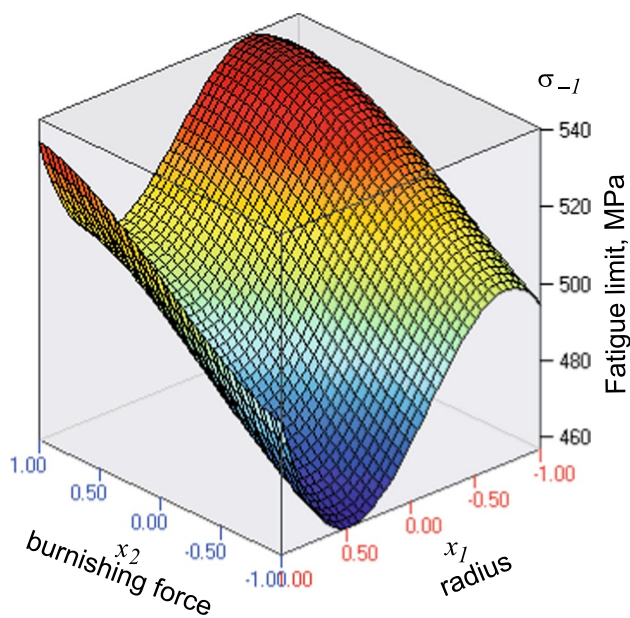
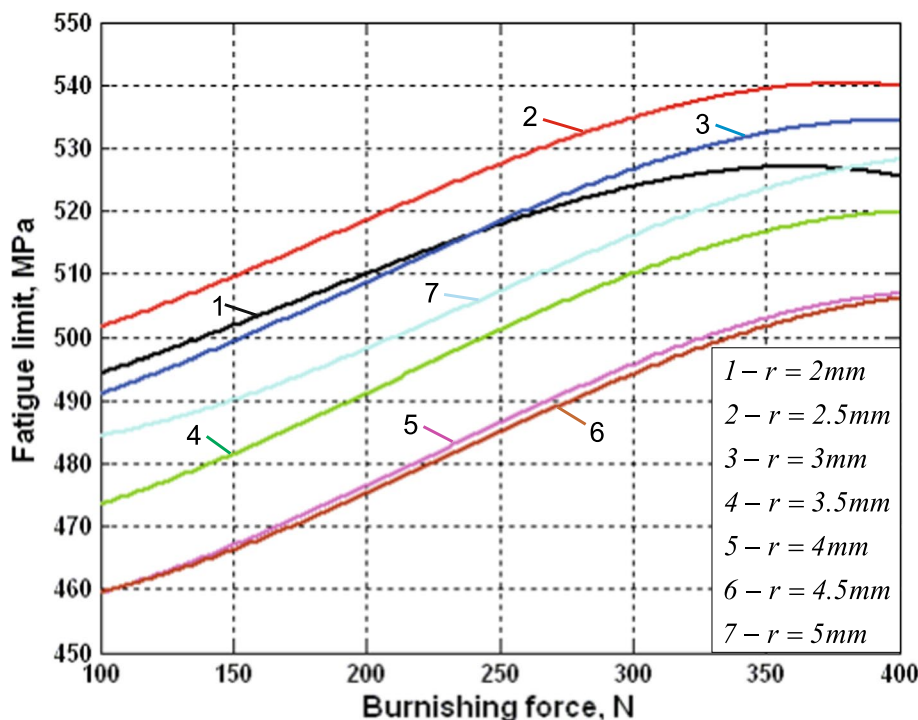


Fig. 16 Dependence of the fatigue limit on the burnishing force and the radius

Fig. 17 Sections of the fatigue limit surface with different planes



SB of 41Cr4 steel with these basic parameters (the number of passes is  $n = 1$  and the working scheme is one-way), the fatigue limit of the processed specimens increased by 22.7%—from 440 to 540 MPa. Figure 13b shows that at a stress amplitude of 540 MPa, the number of cycles to failure is approximately  $10^5$  cycles. Therefore, the fatigue life of the specimens increases more than 100 times after SB with the optimal basic parameters.

## 6.5 Verification of the results obtained

### 6.5.1 Reliability of the approach used

In order to verify the reliability of the approach used to determine the fatigue limit, the result for the sixteenth experimental point (see Table 4) was compared with the fatigue limit obtained via Wöhler's curve (Fig. 18). The average magnitude of the fatigue limit obtained by means

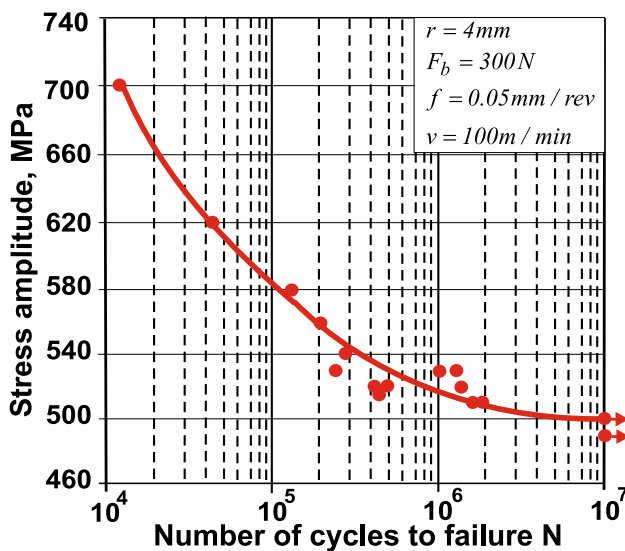
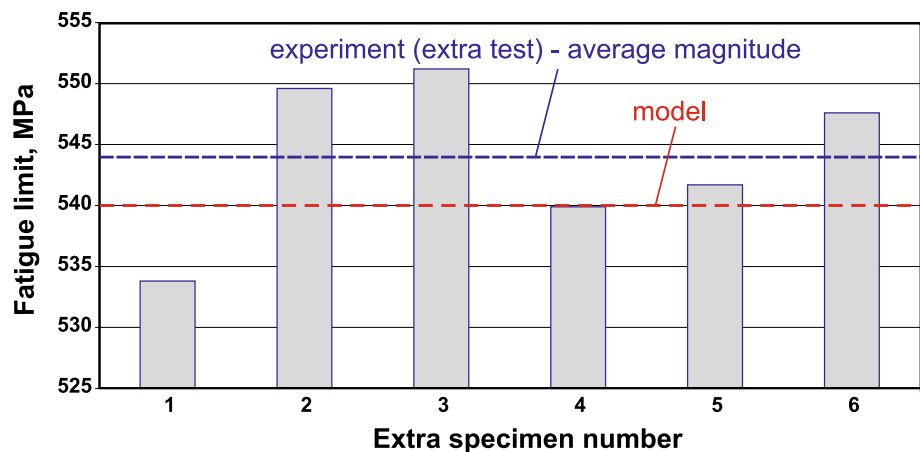


Fig. 18 Fatigue limit obtained via Wöhler's curve

Fig. 19 Comparison between the extra tests and the proposed by the model maximum fatigue limit



of Locatti's method is 491.77 MPa, while Wöhler's curve predicts 500 MPa. The relative deviation (against Wöhler's curve) is 1.6%, demonstrating the reliability of the approach used.

### 6.5.2 The maximum fatigue limit predicted by the model

To verify the maximum fatigue limit predicted by the model (13), six extra fatigue specimens were manufactured using the optimal SB parameters under the "maximum fatigue limit" criterion, namely  $r = 2.5$  mm,  $F_b = 380$  N,  $f = 0.05$  mm/rev and  $v = 100$  m/min. The fatigue limits were obtained via Locatti's method as the arithmetic means of the results from the extra specimens. The comparison between the experimental data (Fig. 19) and the proposed model data indicates good agreement, which proves the authenticity of the model obtained to predict the fatigue limit of slide burnished specimens made of 41Cr4 steel.

## 7 Conclusions

On the basis of the results obtained, the following conclusions can be made:

- An adequate fully coupled thermal-stress FE model was created, and the effects of the basic SB parameters on the introduced residual stresses were studied. It was established that the diamond radius and the burnishing force have the strongest effect on the residual stresses, which, in turn, have a significant influence on the fatigue strength of the corresponding treated component. Large burnishing velocities lead to a large amount of heat being generated, which reduces the beneficial residual stresses in the surface layer. Therefore, the burnishing velocity was limited to  $v = 100$  m/min. With an increase in feed rate, the residual stresses decrease in absolute value; thus  $f = 0.05$  mm/rev was used.

- An extensive experimental investigation of the effects of the selected basic SB parameters on the fatigue limit of the slide burnished specimens was carried out using Locatti's method. The alleged Wöhler's curves and the stepwise increasing stress amplitude were defined in a double logarithmic coordinate system, as the basic (central) curve was obtained in our previous study. Based on a planned experiment, a regression model predicting the fatigue limit was obtained. The maximum deviation (relative error) of the model compared to the experimental results was less than 1.25%. Based on the model obtained, a one-purpose optimization was conducted using a genetic algorithm, and the optimal values for the radius and burnishing force were found.
- Slide diamond burnishing, conducted with the optimal basic parameters under the "maximum fatigue strength" criterion (namely, radius  $r = 2.5$  mm, burnishing force  $F_b = 380$  N, feed rate  $f = 0.05$  mm and burnishing velocity  $v = 100$  m/min) improves the fatigue limit of 37Cr4 steel by 22.7%—from 440 to 540 MPa. The fatigue life increases by more than 100 times. This proves that the SB process is an alternative to deep rolling process.

**Acknowledgement** This work was supported by the European Regional Development Fund within the OP „Science and Education for Smart Growth 2014–2020”, Project CoC “Smart Mechatronics, Eco- and Energy Saving Systems and technologies”, No. BG05M2OP001-1.002-0023.

## References

- Maximov JT, Anchev AP, Duncheva GV, Ganev N, Selimov KF, Dunchev VP (2019) Impact of slide diamond burnishing additional parameters on fatigue behaviour of 2024-T3 Al alloy. *Fatigue Fract Eng Mater Struct* 42(1):363–373
- Maximov JT, Duncheva GV, Anchev AP, Ganev N, Amudjev IM, Dunchev VP (2018) Effect of slide burnishing method on the surface integrity of AISI 316Ti chromium–nickel steel. *J Braz Soc Mech Sci Eng* 40:194. <https://doi.org/10.1007/s40430-018-1135-3>
- Maximov JT, Duncheva GV, Anchev AP, Ichkova MD (2019) Slide burnishing—review and prospects. *Int J Adv Manuf Technol*. <https://doi.org/10.1007/s00170-019-03881-1>
- Balland P, Tabourot L, Degre F, Moreau V (2013) An investigation of the mechanics of roller burnishing through finite element simulation and experiments. *Int J Mach Tools Manuf* 65:29–36
- Balland P, Tabourot L, Degre F, Moreau V (2013) Mechanics of the burnishing process. *Precis Eng* 37:129–134
- Dadmal S, Kurkute V (2017) Finite element analysis of roller burnishing process. *Int Res J Eng Technol* 4(6):2294–2301
- Eshwara PK, Nahavandi S, Mohammed M, Aditiya V (2006) Prediction of residual stresses in roller burnished components—a finite element approach. *Int J Appl Eng Res* 1(2):153–163
- Guo YB, Barkey ME (2004) FE-simulation of the effects of machining-induced residual stress profile on rolling contact of hard machined components. *Int J Mech Sci* 46:371–388
- Klocke F, Bäcker V, Wegner H, Zimmermann M (2011) Finite element analysis of the roller burnishing process for fatigue resistance increase of engine components. *Proc Inst Mech Eng Part B J Eng Manuf* 225(1):2–11
- Kulakowska A (2010) Numerical analysis of the influence of surface asperity vertical angles after turning on the state of stress and strains after part's burnishing rolling. *Logitrans-VII Konferencja Nankowo-Techniczna*, 14–16 April, Szczyrk, Poland, pp 1793–1802
- Malleswara Rao JN, Chennakesava Reddy A, Rama Rao PV (2011) Finite element approach for the prediction of residual stresses in aluminum work pieces produced by roller burnishing. *Int J Des Manuf Technol* 2:7–20
- Patabhi RB, Shashikanth C (2015) Investigations in contact stress analysis in roller burnishing process. *Int J Mag Eng Technol Manag Res* 2(11):1502–1516
- Patyk S, Patyk R, Kukielka L, Kaldunski P, Chojnacki J (2017) Numerical method for determining the main force of burnishing rolling of rough cylindrical surface with regular periodical outlines asperities. In: *23rd International conference engineering mechanics 2017*, Svratka, Czech Republic, 15–18 May 2017, pp 754–757
- Saritha PA (2014) Study on assesment of theories for contact stress distribution at roller-work piece contact in roller burnishing. *Int J Sci Eng Technol Res* 3(1):100–106
- Sartkulvanich P, Altan T, Jasso F, Rodriguez C (2007) Finite element modeling of hard roller burnishing: an analysis on the effects of process parameters upon surface finish and residual stresses. *J Manuf Sci Eng* 129(4):705–716
- Ali M, Michlik P, Pan J (2016) Residual stress distributions in rectangular bars due to high rolling loads. *SAE Int J Mater Manuf* 9(3):661–678
- Beghini M, Bertini L, Monelli BD, Santus S, Bandini M (2014) Experimental parameter sensitivity analysis of residual stresses induced by deep rolling on 7075-T6 aluminium alloy. *Surf Coat Technol* 254:175–186
- Donzella G, Guagliano M, Vergani L (1993) Experimental investigation and numerical analyses on deep rolling residual stresses. *Trans Eng Sci* 2:13–27
- Fonseca L, de Faria A (2018) A deep rolling finite element analysis procedure for automotive crankshafts. *J Strain Anal* 53(3):178–188
- Hassani-Gangaraj S, Carboni M, Gnagliano M (2015) Finite element approach toward an advanced understanding of deep rolling induced residual stresses, and an application to railway axles. *Mater Des* 83:689–703
- Lim A, Castagne S, Wong C (2016) Effect of deep cold rolling on residual stress distributions between the treated and untreated regions on Ti–6Al–4V alloy. *J Manuf Sci Eng* 138(11):111005–111005-8
- Lyubenova N, Baehre D (2015) Finite element modelling and investigation of the process parameters in deep rolling of AISI4140 Steel. *J Mater Sci Eng* 5(7–8):277–287
- Majzooobi GH, Motlagh ST, Amiri A (2010) Numerical simulation of residual stress induced by roll-peening. *Trans Indian Inst Met* 63:499–504
- Manouchehrifar A, Alasvand K (2009) Finite element simulation of deep rolling and evaluate the influence of parameters on residual stress. In: *Recent researches in engineering mechanics, urban & naval transportation and tourism*, pp 61–67
- Manouchehrifar A, Alasvand K (2012) Simulation and research on deep rolling process parameters. *Int J Adv Des Manuf Technol* 5(5):31–37
- Mombeini D, Atrian A (2018) Investigation of deep cold rolling effects on the bending fatigue of brass C38500. *Latin Am J Solid Struct* 15(4):e361-19

27. Perenda J, Trajkovski J, Zerovnik A, Prebil I (2015) Residual stresses after deep rolling of a torsion bar made from high strength steel. *J Mater Process Technol* 218:89–98
28. Rodríguez A, López de Lacalle LN, Celaya A, Lamikiz A, Albizuri J (2012) Surface improvement of shafts by the deep ball-burnishing technique. *Surf Coat Technol* 206:2817–2824
29. Trauth D, Klocke F, Mattfeld P, Klink A (2013) Time-efficient prediction of the surface layer state after deep rolling using similarity mechanics approach. *Proc CIRP* 9:29–34
30. Uddin MS, Hall C, Hooper R, Charrault E, Murphy P, Santos V (2018) Finite element analysis of surface integrity in deep ball-burnishing of a biodegradable AZ31B Mg. *Metals* 136(8):1–17
31. Aldrine ME, Mahendra Babua NC, Anil KS (2017) Evaluation of induced residual stresses due to low plasticity burnishing through finite element simulation. *Mater Today Proc* 4:10850–10857
32. Beres W, Patnaik P, Li J (2004) Numerical simulation of the low plasticity burnishing process for fatigue property enhancement. In: *Proceedings of the ASME Turbo Expo 2004, Power and Land, Sea and Air, June 14–17, 2004, Vienna, Austria*
33. Fu CH, Guo YB, McKinney J, Wei XT (2012) Process mechanics of low plasticity burnishing of nitinol alloy. *J Mater Eng Perform* 21:2607–2617
34. Hassanifard S, Mousavi M, Varvani-Farahani A (2019) The influence of low-plasticity burnishing process on the fatigue life of friction-stir-processed Al7075-T6 samples. *Fatigue Fract Eng Mater Struct* 42(3):764–772
35. Li FL, Xia W, Zhou ZY (2010) Finite element calculation of residual stress and cold-work hardening induced in Inconel 718 by low plasticity burnishing. In: *Third international conference on information and computing, Wuxi, China, 4–6 June 2010*
36. Mohammadi F, Sedaghati R, Bonakdar A (2014) Finite element analysis and design optimization of low plasticity burnishing process. *Int J Adv Manuf Technol* 70(5–8):1337–1354
37. Zhuang W, Wicks B (2004) Multipass low-plasticity burnishing induced residual stresses: three-dimensional elastic-plastic finite element modeling. *Proc Inst Mech Eng Part C J Mech Eng Sci* 218(6):663–668
38. He D, Wang B, Zhang J, Liao S, Deng WJ (2018) Investigation of interference effect on the burnishing process. *Int J Adv Manuf Technol* 95:1–10
39. Maximov JT, Duncheva GV (2012) Finite element analysis and optimization of spherical motion burnishing of low-alloy steel. *Proc IMechE Part C J Mech Eng Sci* 226(1):161–176
40. Maximov JT, Duncheva GV, Anchev AP, Dunchev VP (2019) Crack resistance enhancement of joint bar holes by slide diamond burnishing using new tool equipment. *Int J Adv Manuf Technol*. <https://doi.org/10.1007/s00170-019-03405-x>
41. Maximov JT, Anchev AP, Duncheva GV, Ganev N, Selimov KF (2017) Influence of the process parameters on the surface roughness, micro-hardness, and residual stresses in slide burnishing of high-strength aluminum alloys. *J Braz Soc Mech Sci Eng* 39(8):3067–3078
42. Maximov JT, Duncheva GV, Anchev AP, Amudjev IM, Kuzmanov VT (2014) Enhancement of fatigue life of railend-bolt holes by slide diamond burnishing. *Eng Solid Mech* 2(4):247–264
43. Maximov JT, Anchev AP, Dunchev VP, Ganev N, Duncheva GV, Selimov KF (2017) Effect of slide burnishing basic parameters on fatigue performance of 2024-T3 high-strength aluminium alloy. *Fatigue Fract Eng Mater Struct* 40(11):1893–1904
44. Maximov JT, Duncheva GV, Anchev AP (2019) A temperature-dependent, non-linear kinematic/isotropic hardening material constitutive model of the surface layer of 37Cr4 steel subjected to slide burnishing. *Arab J Sci Eng*. <https://doi.org/10.1007/s1336-9-019-03765-2>
45. Teimouri R, Amini S, Bami AB (2018) Evaluation of optimized surface properties and residual stress in ultrasonic assisted ball burnishing of AA6061-T6. *Measurement* 116:129–139
46. Kuznetsov V, Smolin I, Dmitriev A, Kononov D, Makarov A, Kiryakov A, Yurovskikh A (2013) Finite element simulation of nanostructuring burnishing. *Phys Mesomech* 16(1):62–72
47. Aliev KT, Aslanov TI (1979) The influence of diamond burnishing on the fatigue strength and wear resistance of the shafts of petroleum chains. *Chem Pet Eng* 15(6):459–461
48. Korzynski M, Lubas J, Swirad S, Dudek K (2011) Surface layer characteristics due to slide diamond burnishing with a cylindrical ended tool. *J Mater Process Technol* 211:84–94
49. Korzynski M, Pacana A, Cwanek J (2009) Fatigue strength of chromium coated elements and possibility of its improvement with slide diamond burnishing. *Surf Coat Technol* 203:1670–1676
50. Maximov JT, Duncheva GV, Anchev AP, Ganev N, Dunchev VP (2019) Effect of cyclic loading on fatigue performance of slide burnishing components made of low-alloy medium carbon steel. *Fatigue Fract Eng Mater Struct*. <https://doi.org/10.1111/ffe.13001>
51. Swirad S (2007) The effect of burnishing parameters on steel fatigue strength. *Nonconv Technol Rev* 1:113–118
52. Maximov JT, Anchev AP, Duncheva GV (2015) Modeling of the friction in tool-workpiece system in diamond burnishing process. *Coupled Syst Mech* 4(4):279–295
53. Reemsnyder HS (1961) The fatigue behavior of structural steel weldments—a literature survey, Lehigh University, (November 1961) 152p. Fritz Laboratory Reports. Paper 1818
54. Vuchkov IN, Vuchkov II (2009) QStatLab Professional, v. 5.5-statistical quality control software. User's manual, Sofia

**Publisher's Note** Springer Nature remains neutral with regard to jurisdictional claims in published maps and institutional affiliations.